Article

Enhanced Photocatalytic Performance and Mechanism of Au@CaTiO$_3$ Composites with Au Nanoparticles Assembled on CaTiO$_3$ Nanocuboids

Yuxiang Yan [1], Hua Yang [1,*], Zao Yi [2], Ruishan Li [1] and Xiangxian Wang [1]

1   State Key Laboratory of Advanced Processing and Recycling of Non-ferrous Metals, Lanzhou University of Technology, Lanzhou 730050, China; yanyx@lut.cn (Y.Y.); liruishan@lut.cn (R.L.); wangxx869@lut.edu.cn (X.W.)
2   Joint Laboratory for Extreme Conditions Matter Properties, Southwest University of Science and Technology, Mianyang 621010, China; yizaomy@swust.edu.cn
*   Correspondence: hyang@lut.cn; Tel.: +86-931-2973-783

check for updates

Abstract: Using P25 as the titanium source and based on a hydrothermal route, we have synthesized CaTiO$_3$ nanocuboids (NCs) with the width of 0.3–0.5 μm and length of 0.8–1.1 μm, and systematically investigated their growth process. Au nanoparticles (NPs) of 3–7 nm in size were assembled on the surface of CaTiO$_3$ NCs via a photocatalytic reduction method to achieve excellent Au@CaTiO$_3$ composite photocatalysts. Various techniques were used to characterize the as-prepared samples, including X-ray powder diffraction (XRD), scanning/transmission electron microscopy (SEM/TEM), diffuse reflectance spectroscopy (UV-vis DRS), Fourier transform infrared spectroscopy (FTIR), and X-ray photoelectron spectroscopy (XPS). Rhodamine B (RhB) in aqueous solution was chosen as the model pollutant to assess the photocatalytic performance of the samples separately under simulated-sunlight, ultraviolet (UV) and visible-light irradiation. Under irradiation of all kinds of light sources, the Au@CaTiO$_3$ composites, particularly the 4.3%Au@CaTiO$_3$ composite, exhibit greatly enhanced photocatalytic performance when compared with bare CaTiO$_3$ NCs. The main roles of Au NPs in the enhanced photocatalytic mechanism of the Au@CaTiO$_3$ composites manifest in the following aspects: (1) Au NPs act as excellent electron sinks to capture the photoexcited electrons in CaTiO$_3$, thus leading to an efficient separation of photoexcited electron/hole pairs in CaTiO$_3$; (2) the electromagnetic field caused by localized surface plasmon resonance (LSPR) of Au NPs could facilitate the generation and separation of electron/hole pairs in CaTiO$_3$; and (3) the LSPR-induced electrons in Au NPs could take part in the photocatalytic reactions.

Keywords: CaTiO$_3$ nanocuboids; Au nanoparticles; localized surface plasmon resonance; Au@CaTiO$_3$ composite; photocatalytic performance

1. Introduction

The rapid social development has raised two big issues facing mankind, i.e., environmental pollution and energy shortage. In particular, water resources are seriously and increasingly becoming polluted by the wastewater discharged from chemical industries, which poses a great threat to human health and survival. Organic dyes and pigments, most commonly existing in the industrial wastewater, are carcinogenic to humans and hardly self-decomposed [1,2]. It is imperative to remove the organic pollutants and purify water resources via a simple, low-cost, green and non-fossil-consumptive technology. In this sense, semiconductor-based photocatalysis has sparked a great interest due to its potential applications in wastewater treatment [3–8]. This technology allows the use of solar light—a sustainable, inexhaustible and economically attractive energy source—as the power source to degrade

organic pollutants. The photocatalytic process depends highly on photogenerated electrons (e$^-$) and holes (h$^+$) in semiconductor photocatalysts, as well as their reduction and oxidation capabilities. Nevertheless, the photoexcited e$^-$/h$^+$ pairs are easily to be recombined and only a few of them are available for the photocatalytic reactions. To achieve an excellent semiconductor photocatalyst, the photoexcited e$^-$/h$^+$ pairs must be efficiently separated. As an important class of photocatalysts, titanium-contained oxide semiconductors can be photocatalytically active only under ultraviolet (UV) irradiation owing to their wide bandgap (E_g = 3.1–3.3 eV) [9–13]. It is noted that solar radiation includes only a small portion of UV light (~5%), but a large amount of visible light (45%). Enhancing the visible-light absorption of photocatalysts is the key point to make the best use of solar energy to drive the photocatalysis. Up to now, various strategies have been widely applied to modify semiconductor photocatalysts with the aim of facilitating the photoexcited e$^-$/h$^+$ pair separation and widening their light absorption range [14–20].

Zero-dimensional, one-dimensional and two-dimensional nanomaterials (e.g., metal nanoparticles (NPs), carbon quantum dots, carbon nanotubes, graphene) have attracted a great deal of interest due to their interesting physicochemical characteristics and great potential applications in the fields of bioimaging, energy conversion, optoelectronic devices, wave absorption and sensors [21–33]. Furthermore, these nanomaterials can be used as excellent modifiers or co-catalysts and are widely coupled with semiconductors to improve their photocatalytic performances [34–38]. Noble metal NPs are particularly interesting as the co-catalysts because they can not only facilitate the photoexcited e$^-$/h$^+$ pair separation but also enhance visible-light absorption. The enhanced photocatalytic mechanisms by noble metal NPs can be ascribed to two aspects [39,40]. First, noble metal NPs can act as electron sinks to trap photogenerated electrons from the semiconductor, thus leading to an efficient separation of e$^-$/h$^+$ pairs. Second, noble metal NPs can absorb visible light to induce localized surface plasmon resonance (LSPR) [41,42]. The LSPR-caused electromagnetic field could facilitate the generation and separation of e$^-$/h$^+$ pairs in the semiconductor. Simultaneously, LSPR-induced electrons in noble metal NPs could also take part in the photocatalytic reactions. Due to these unique properties, much work has demonstrated that noble metal NPs decorated semiconductors manifest significantly enhanced photocatalytic performances when compared with bare semiconductors [15,38–40].

Calcium titanate (CaTiO$_3$), a typical titanium-contained oxide semiconductor with a perovskite-type structure, has sparked a great interest among researchers owing to its promising properties of ferroelectricity, piezoelectricity, elasticity, and photocatalytic activity [43–47]. As a photocatalyst, CaTiO$_3$ has been shown to exhibit a pronounced photocatalytic degradation of organic pollutants, as well as photocatalytic splitting of water into hydrogen and oxygen [48–52]. Semiconductor-based photocatalysis, intrinsically being a heterogeneous surface catalytic reaction, is highly dependent on the crystal morphology of the semiconductor. In particular, an excellent photocatalytic activity could be achieved for the semiconductor with special exposed facets [53,54]. In our previous studies, we have demonstrated that CaTiO$_3$ nanocuboids (NCs) with (101) and (010) exposed facets exhibit a photocatalytic activity superior to that of sphere-like CaTiO$_3$ nanoparticles [55]. In this work, we have assembled Au NPs on the surface of CaTiO$_3$ NCs and found that the obtained Au@CaTiO$_3$ composites exhibit much enhanced photocatalytic degradation of organic dyes under both UV and visible light irradiation. Compared to Ag NPs, Au NPs offer an advantage of higher chemical stability. However, there is no work concerned with the Au NPs modified CaTiO$_3$ photocatalysts, though Ag NPs have been frequently used as a co-catalyst to improve the photocatalytic performance of CaTiO$_3$ [56–58]. Here we also systematically investigated the growth process of CaTiO$_3$ photocatalysts. The photocatalytic mechanism of the Au@CaTiO$_3$ composites were systematically investigated and discussed. The present Au@CaTiO$_3$ nanocomposite photocatalysts can be introduced in micro/nano photocatalytic devices for the wastewater treatment.

2. Materials and Methods

2.1. Synthesis of CaTiO$_3$ NCs

CaTiO$_3$ NCs were synthesized via a hydrothermal route at 200 °C as described in the literature [55]. To unveil the growth process of CaTiO$_3$ NCs, different hydrothermal reaction times (0.5, 1, 5, 10 and 24 h) were performed.

2.2. Assembly of Au NPs on CaTiO$_3$ NCs

A photocatalytic reduction method was employed to hybridize Au NPs on the surface of CaTiO$_3$ NCs synthesized at 200 °C for 24 h. 0.1 g of the as-synthesized CaTiO$_3$ NCs and 0.025 g of ammonium oxalate (AO) were successively added in 80 mL of deionized water. The suspension was ultrasonically treated for 30 min and then magnetically stirred for another 30 min to make CaTiO$_3$ particles uniformly disperse. 0.8 mL of HAuCl$_4$ solution (0.029 mol·L^{-1}, M) was dropped in the CaTiO$_3$ suspension. The resultant mixture was magnetically stirred for 60 min, and then irradiated with ultraviolet (UV) light, which was emitted from a 15 W low-pressure mercury lamp, for 30 min under mild stirring. During the irradiation process, Au^{3+} ions were reduced by the photogenerated electrons in CaTiO$_3$ to form Au NPs, which were simultaneously assembled on the surface of CaTiO$_3$ NCs. The product was collected by centrifugation. After washing several times with deionized water and ethanol, and then drying at 60 °C for 12 h, the final product was obtained as the 4.3%Au@CaTiO$_3$ composite with an Au mass fraction of 4.3%. By adding different volumes of HAuCl$_4$ solution (0.2, 0.5, 1.1 and 1.4 mL), several other composite samples 1.1%Au@CaTiO$_3$, 2.7%Au@CaTiO$_3$, 5.9%Au@CaTiO$_3$ and 7.4%Au@CaTiO$_3$ were also prepared.

2.3. Sample Characterization

The crystal structures, morphologies and microstructures of the samples were characterized by X-ray powder diffraction (XRD) and scanning/transmission electron microscopy (SEM/TEM). The used apparatuses were a D8 Advance X-ray diffractometer (Bruker AXS, Karlsruhe, Germany), a JSM-6701F field-emission scanning electron microscope (JEOL Ltd., Tokyo, Japan) and a JEM-1200EX field-emission transmission electron microscope (JEOL Ltd., Tokyo, Japan). A PHI-5702 multi-functional X-ray photoelectron spectrometer (Physical Electronics, hanhassen, MN, USA) was employed for the X-ray photoelectron spectroscopy (XPS) analysis. Ultraviolet-visible (UV-vis) diffuse reflectance spectroscopy (DRS) measurements were performed on a TU-1901 double beam UV-vis spectrophotometer (Beijing Purkinje General Instrument Co. Ltd., Beijing, China). A Spectrum Two Fourier transform infrared (FTIR) spectrophotometer (PerkinElmer, Waltham, MA, USA) was used for the FTIR spectroscopy analysis of the samples.

2.4. Photocatalytic Test

To assess the photocatalytic performances of the samples, RhB in aqueous solution (5 mg·L^{-1}) was used as the model pollutant. Simulated sunlight (emitted from a 200 W xenon lamp, 300 < λ < 2500 nm), UV light (emitted from a 30 W low-pressure mercury lamp, λ = 254 nm) and visible light (generated by a 200 W halogen-tungsten lamp, λ > 400 nm) were separately used as the light source. The reaction solution was composed of 100 mL of RhB solution and 0.1 g of the photocatalyst. The adsorption of RhB on the photocatalyst surface was examined by magnetically stirring the mixture in the dark for 30 min. The RhB concentration was monitored by measuring the absorbance of the reaction solution. 2.5 mL of the reaction solution was sampled from the photoreactor and centrifuged to remove the photocatalyst. The absorbance measurement was performed on a UV-vis spectrophotometer at λ = 554 nm. The percentage degradation of RhB (*D*%) was obtained according to $D\% = (C_0 - C_t)/C_0 \times 100\%$ (C_0 = initial RhB concentration; C_t = residual RhB concentration).

3. Results and Discussion

3.1. Synthesis and Growth Process of CaTiO₃ NCs

The crystal structures of precursor P25 and the samples prepared at 200 °C with different reaction times (0.5, 1, 5, 10 and 24 h) were determined by XRD patterns, as shown in Figure 1. It is seen that at 0.5 h reaction time, the obtained sample maintains a crystal structure identical to that of P25 without the formation of $CaTiO_3$ phase. At 1 h reaction time, $CaTiO_3$ phase is largely crystallized and only minor TiO_2 is observed in the resultant sample. When the reaction time is increased up to 5 h, single $CaTiO_3$ phase is obtained. All the diffraction peaks of the sample can be indexed to the $CaTiO_3$ orthorhombic phase (JCPDS#42-0423). With further prolonging the reaction time, the diffraction peaks of the resultant samples undergo no change, indicating no structural change of $CaTiO_3$ crystals.
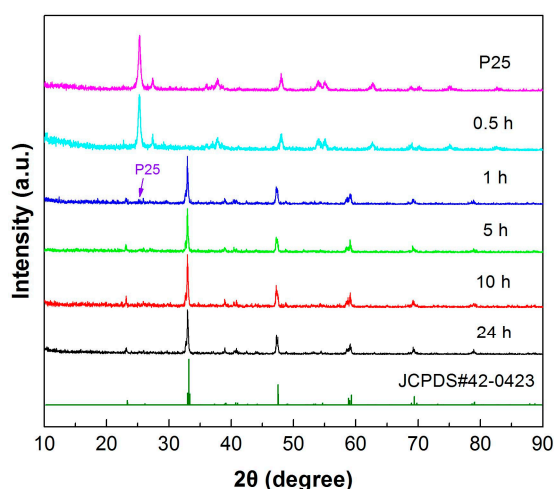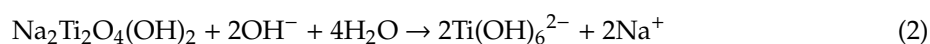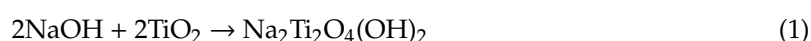

Figure 1. X-ray powder diffraction (XRD) patterns of precursor P25 and the samples prepared at 200 °C with different reaction times (0.5, 1, 5, 10 and 24 h).

Figure 2 illustrates the SEM images of precursor P25 and the samples prepared at different reaction times. It is seen that P25 is composed of sphere-like nanoparticles with average size of 25 nm (Figure 2a). At 0.5 h of reaction, the TiO_2 nanoparticles undergo almost no change, as shown in Figure 2b. The sample derived at 1 h reaction time mainly consists of cuboid-like particles together with minor sphere-like nanoparticles (Figure 2c), indicating that most of TiO_2 nanoparticles are coupled with Ca species to form $CaTiO_3$ NCs. With increasing the reaction time up to 5 h, TiO_2 nanoparticles disappear and single $CaTiO_3$ NCs are formed, as depicted in Figure 2d. These $CaTiO_3$ NCs have a size of 0.3–0.5 μm in width and 0.8–1.1 μm in length. Further prolonging the reaction time up to 10 h (Figure 2e) and 24 h (Figure 2f) leads to no obvious morphological change of $CaTiO_3$ NCs.

The growth process and mechanism of $CaTiO_3$ NCs is schematically illustrated in Figure 3. In the concentrated NaOH solution, polycrystalline TiO_2 nanoparticles are expected to react with NaOH to form $Na_2Ti_2O_4(OH)_2$ particles [59]. Simultaneously, in the strong alkaline environment and high temperature-high pressure conditions, $Na_2Ti_2O_4(OH)_2$ dissociates to form $Ti(OH)_6^{2-}$ ion groups [60]. Ca^{2+} ions in the precursor solution are adsorbed onto the surface of $Ti(OH)_6^{2-}$ ions and further penetrate into the interior. During this process, a series of chemical reactions will take place, including the breaking of Ti-O-Ti bonds, dehydroxylation and nucleation of $CaTiO_3$ crystals. To reduce the overall surface energy, the nucleated $CaTiO_3$ crystals grow into nanocuboids finally. The dominant chemical reactions involved can be briefly described as follows:
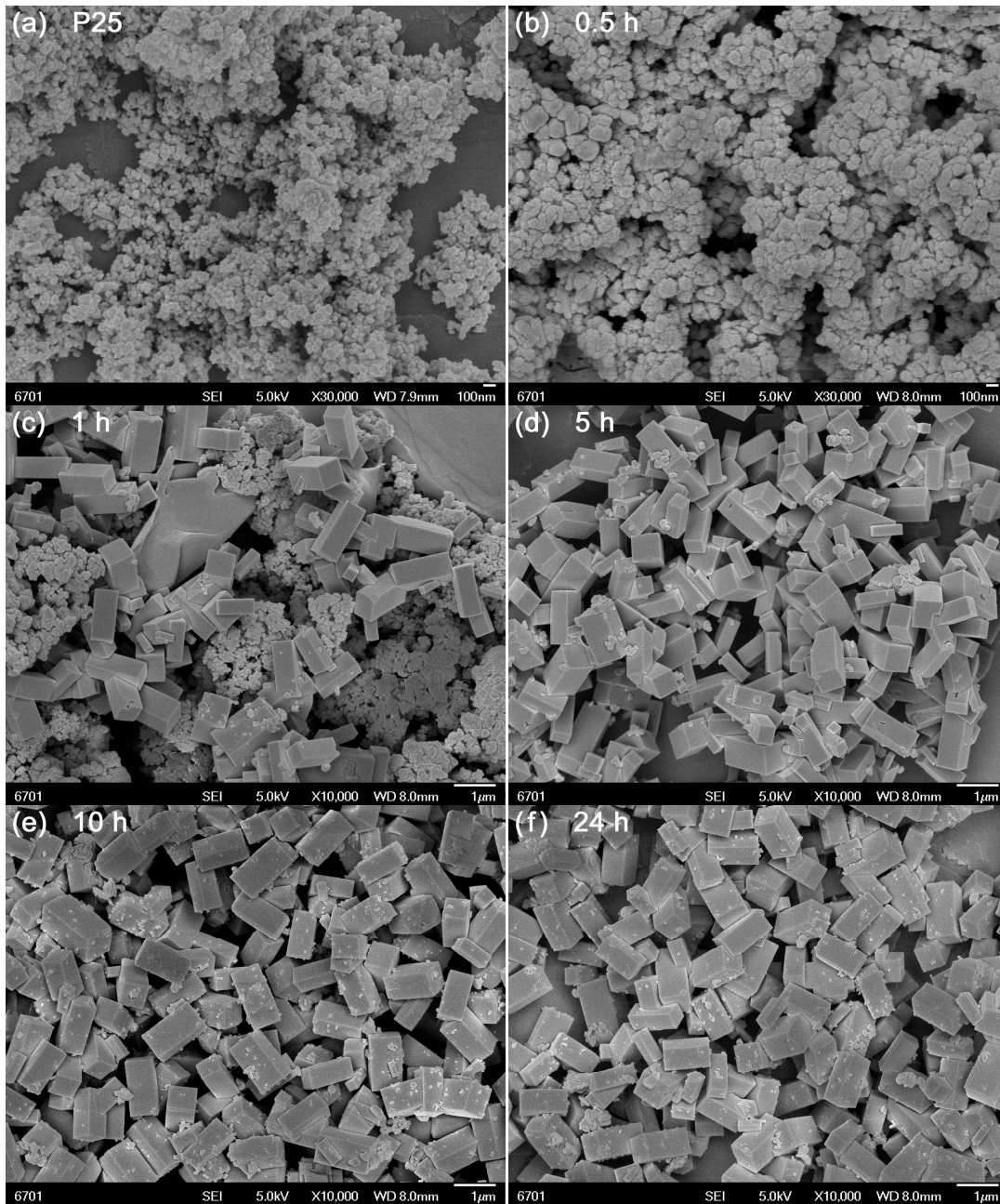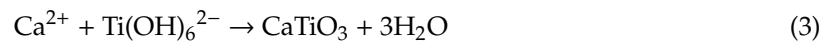
$$2NaOH + 2TiO_2 \rightarrow Na_2Ti_2O_4(OH)_2 \tag{1}$$

$$Na_2Ti_2O_4(OH)_2 + 2OH^- + 4H_2O \rightarrow 2Ti(OH)_6^{2-} + 2Na^+ \tag{2}$$

$$Ca^{2+} + Ti(OH)_6{}^{2-} \rightarrow CaTiO_3 + 3H_2O \qquad (3)$$

Figure 2. Scanning electron microscopy (SEM) images of (**a**) precursor P25 and the samples prepared at (**b**) 0.5, (**c**) 1, (**d**) 5, (**e**) 10 and (**f**) 24 h.
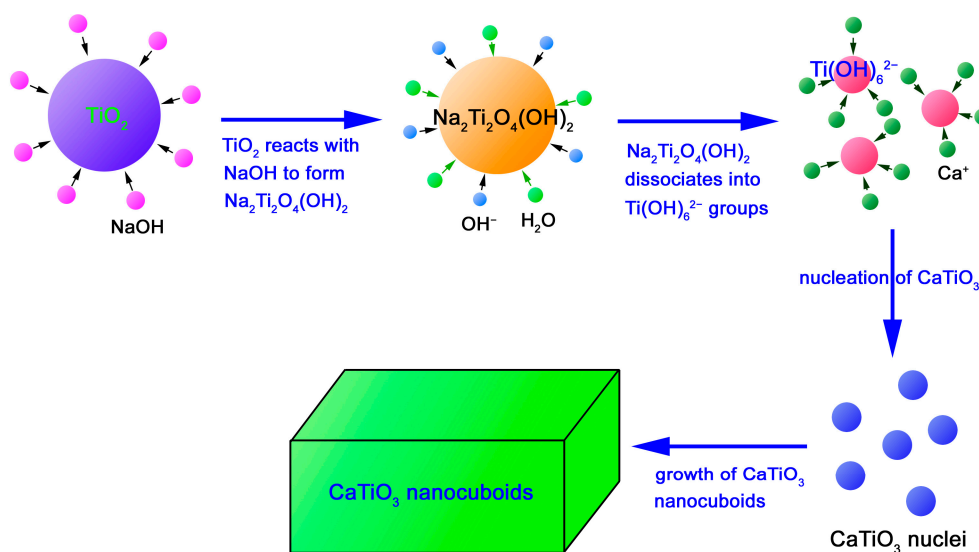
Figure 3. Schematic illustration of the growth process and mechanism of CaTiO₃ NCs.

3.2. Au NPs Modified CaTiO₃ NCs

CaTiO₃ NCs synthesized at 200 °C for 24 h was chosen to be modified with Au NPs with the aim of enhancing their photocatalytic performance. Figure 4 shows the XRD patterns of bare CaTiO₃ NCs and 4.3%Au@CaTiO₃ composite. The dominant diffraction peaks of 4.3%Au@CaTiO₃ are similar to those of bare CaTiO₃, indicating that the CaTiO₃ orthorhombic structure undergoes no change on the decoration of Au NPs. However, additional weak diffraction peaks characterized as the Au cubic structure (JCPDS#04-0784) are clearly detected on the XRD pattern of the composite, which confirms the formation of Au NPs onto CaTiO₃ NCs.
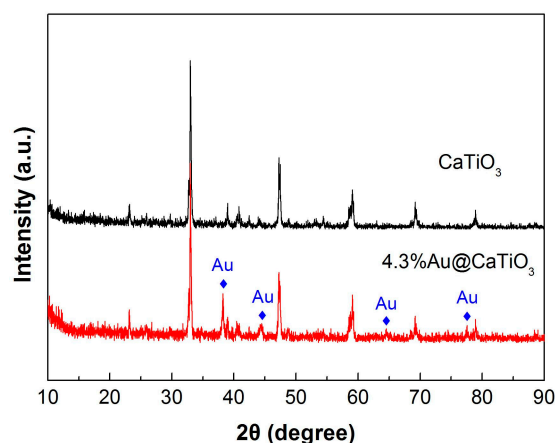

Figure 4. XRD patterns of bare CaTiO₃ NCs and the 4.3%Au@CaTiO₃ composite.

TEM investigation was further carried out to unveil the microstructure of the 4.3%Au@CaTiO₃ composite. Figure 5a shows the TEM image of the composite, from which one can see that CaTiO₃ presents a regular morphology of NCs with width of 0.3–0.5 μm and length of 0.8–1.1 μm. The CaTiO₃ morphology obtained by TEM is in accordance with the SEM observation result. Moreover, small-sized Au NPs are seen to be decorated on the surface of CaTiO₃ NCs. The high-resolution TEM (HRTEM) image depicted in Figure 5b further confirms the good assembly of Au NPs on the surface of CaTiO₃ NCs. The decorated Au NPs are shaped like spheres and have a size distribution of 3–7 nm. Energy-dispersive x-ray elemental mapping was used to investigate the elemental distribution of the 4.3%Au@CaTiO₃ composite. Figure 5c illustrates the dark-field scanning TEM (DF-STEM) image of the composite, and the corresponding elemental mapping images are given in Figure 5d–g. It is observed that the

NCs present uniformly-distributed elements of Ca, Ti and O. Moreover, Au element is also seen to be uniformly distributed throughout the NCs, indicating that $CaTiO_3$ NCs are uniformly decorated with Au NPs. Energy-dispersive X-ray spectroscopy (EDS) spectrum was further used to examine the chemical composition of the 4.3%Au@$CaTiO_3$ composite. As shown in Figure 5h, the composite sample is composed of Ca, Ti, O, and Au elements. Additional Cu and C signals detected on the EDS spectrum could come from the TEM microgrid holder [61]. The obtained Au content from the EDS spectrum is 4.1%, which is basically in agreement with the stoichiometric composition of the 4.3%Au@$CaTiO_3$ composite.

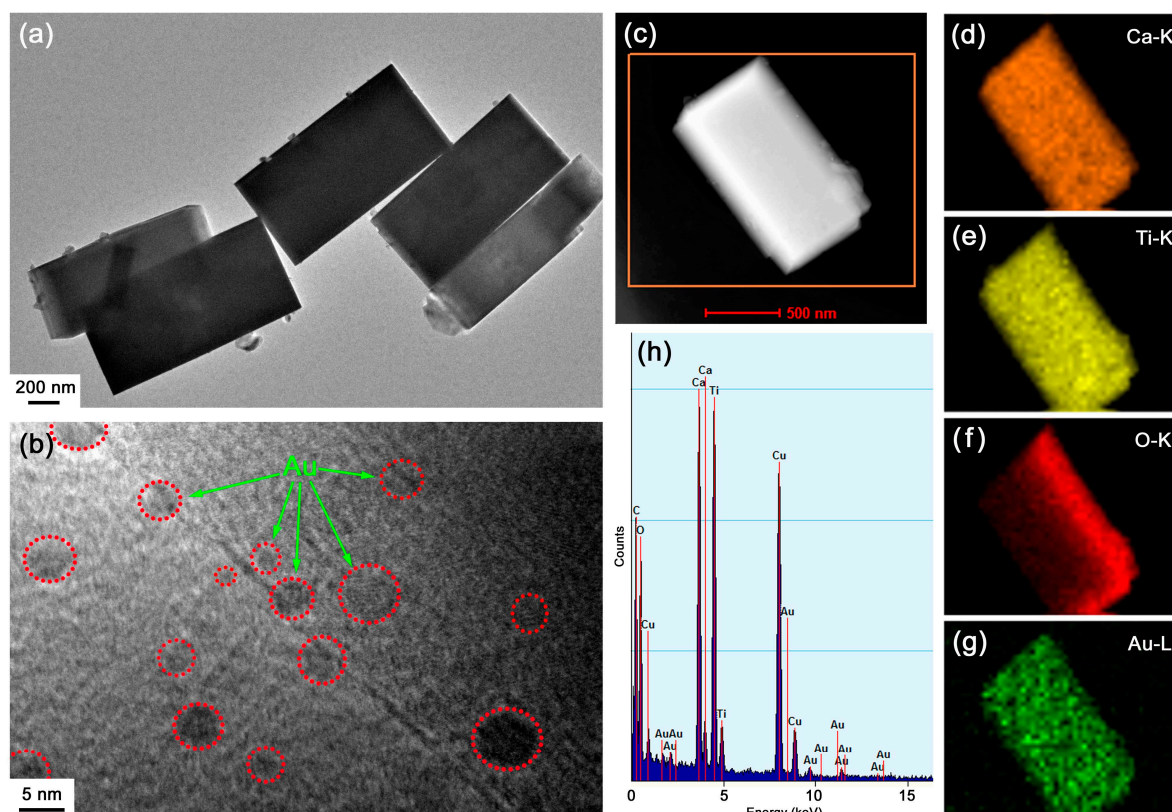**Figure 5.** Transmission electron microscopy (TEM) image (**a**), HRTEM image (**b**), DF-STEM image (**c**), elemental mapping images (**d**–**g**), and EDS spectrum (**h**) of the 4.3%Au@$CaTiO_3$ composite.

The XPS analyses were performed on 4.3%Au@$CaTiO_3$ to elucidate the chemical states of elements. Figure 6a shows the survey XPS spectrum, revealing that the composite is composed of the elements Ca, Ti, O and Au. The observed C signal comes from adventitious carbon, which is used for the calibration of binding energy (C 1s binding energy: 284.8 eV). On the high-resolution XPS spectrum of Ca 2p core level (Figure 6b), the observed peaks at 346.7 and 350.2 eV account for Ca 2p$_{3/2}$ and Ca 2p$_{1/2}$, respectively. On the Ti 2p XPS spectrum (Figure 6c), the Ti 2p$_{3/2}$ and Ti 2p$_{1/2}$ binding energies are observed at 458.8 and 464.4 eV, respectively. The binding energy positions suggest that the Ca and Ti species behave as Ca^{2+} and Ti^{4+} oxidation states, respectively [13]. Two peaks at 529.9 and 532.1 eV are detected on the O 1s XPS spectrum (Figure 6d), which are assigned to the crystal lattice oxygen in $CaTiO_3$ and chemisorbed oxygen species [13,62]. On the Au 4f XPS spectrum (Figure 6e), the peak at 83.6 is attributed to Au 4f$_{7/2}$ and the peak at 87.2 eV corresponds to Au 4f$_{5/2}$. This implies the Au species exists in the metallic state [63].
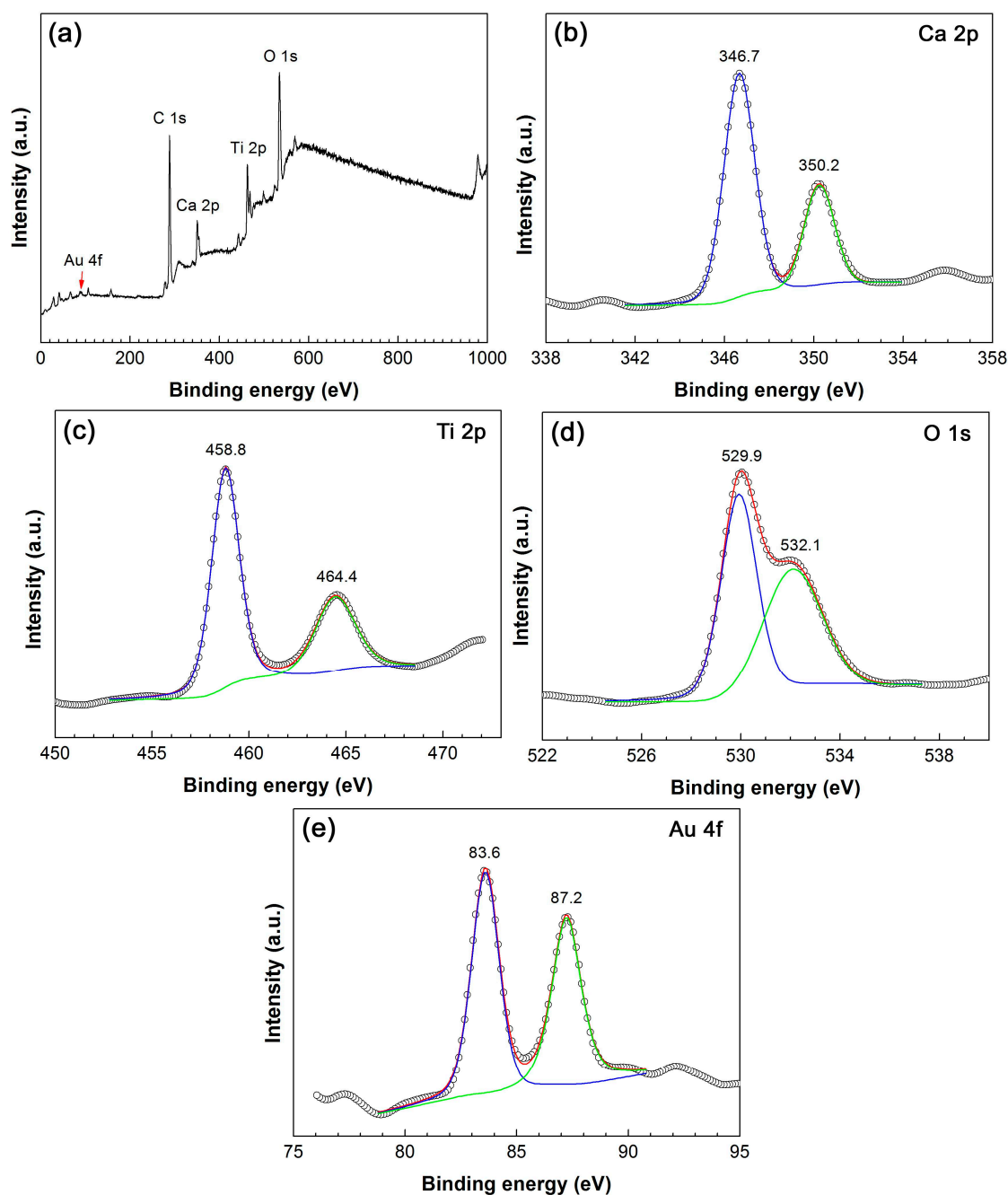
Figure 6. XPS survey scan spectrum (**a**), and high-resolution XPS spectra of (**b**) Ca 2p, (**c**) Ti 2p, (**d**) O 1s and (**e**) Au 4f of the 4.3%Au@CaTiO$_3$ composite.

Figure 7a,b depict the UV-vis DRS spectra of CaTiO$_3$ and 4.3%Au@CaTiO$_3$, respectively, along with the corresponding first derivative curves of the UV-vis DRS spectra and the digital images of the samples (insets). It is seen that the decoration of Au NPs onto CaTiO$_3$ NCs obviously enhances the visible-light absorption. This is further confirmed by the deepening of the apparent color for the 4.3%Au@CaTiO$_3$ composite (dark gray), as compared to bare CaTiO$_3$ NCs (cream white). The enhanced visible-light absorption implies that the Au@CaTiO$_3$ composite photocatalyst can utilize photons more effectively. From the first derivative spectra, the absorption edge of CaTiO$_3$ and 4.3%Au@CaTiO$_3$ is obtained as 369.3 and 355.0 nm, respectively [64]. This suggests that bare CaTiO$_3$ has a bandgap energy (E_g) of 3.36 eV and 4.3%Au@CaTiO$_3$ exhibits an E_g of 3.49 eV. The slight increase in the E_g of the composite could be due to the interaction between CaTiO$_3$ NCs and Au NPs.

We measured the FTIR spectra of $CaTiO_3$ and 4.3%Au@$CaTiO_3$ to elucidate their functional groups, as shown in Figure 8. The absorption peaks at 437 and 560 cm^{-1} are characterized as the Ti–O stretching vibration and Ti–O–Ti bridging stretching mode [65,66]. This implies the existence of TiO_6 octahedra and the formation of $CaTiO_3$ perovskite-type structure. The observed broad bands at 3430 (H_2O stretching vibration) and 1637 cm^{-1} (H_2O bending vibration) suggest the presence of water molecules absorbed on the surface of the samples [67]. The presence of NH^{3+} group can be confirmed by the N–H stretching vibration located at around 3146 cm^{-1} [68]. The peaks detected at 1395 and 1102 cm^{-1} are attributed to the O–H in-plane deformation and C–OH stretching vibrations of alcohols [34]. This indicates that alcohols could be anchored on the samples during their washing process. In addition, no characteristic peaks assignable to Au oxides are observed for the 4.3%Au@$CaTiO_3$ composite, implying Au species exists in the metallic state.
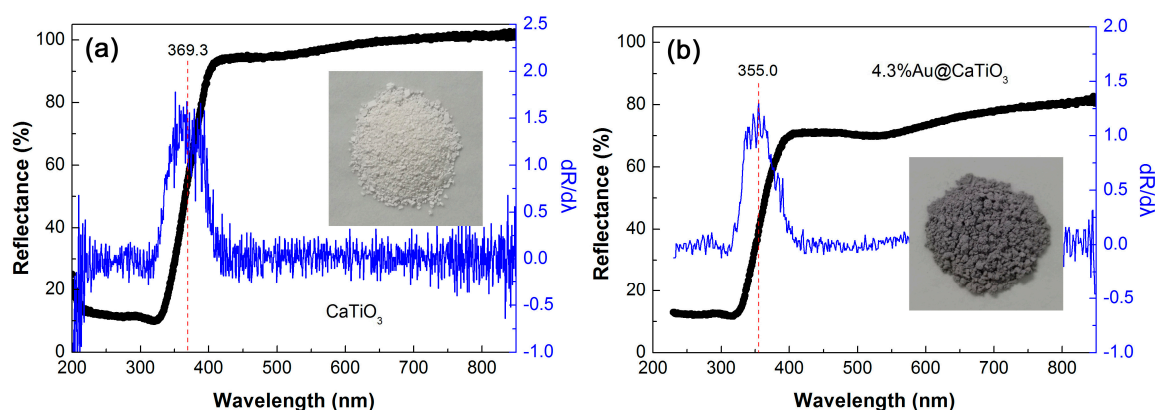

Figure 7. UV-vis diffuse reflectance spectroscopy (DRS) spectra, first derivative curves of the UV-vis DRS spectra and digital images (insets) of (**a**) $CaTiO_3$ and (**b**) 4.3%Au@$CaTiO_3$.

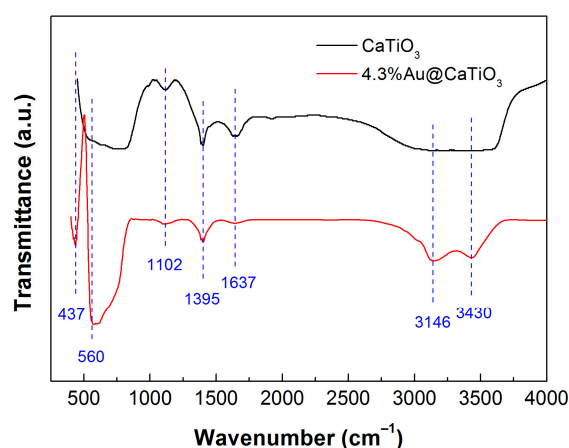**Figure 8.** Fourier transform infrared spectroscopy (FTIR) spectra of $CaTiO_3$ and 4.3%Au@$CaTiO_3$.

To assess the photocatalytic degradation of RhB over the samples, three types of light source were separately used, i.e., simulated sunlight (300 < λ < 2500 nm), UV light (λ = 254 nm) and visible light (λ > 400 nm). Figure 9a shows the simulated-sunlight degradation of RhB photocatalyzed by $CaTiO_3$ and Au@$CaTiO_3$ composites. It is demonstrated that the Au@$CaTiO_3$ composites manifests a photocatalytic activity much superior to that of bare $CaTiO_3$ NCs. The content of decorated Au NPs has an obvious effect on the photocatalytic activity of the composite samples. With increasing the Au content, the photocatalytic activity of the samples gradually increases and reaches the highest level for 4.3%Au@$CaTiO_3$. However, further increasing the Au content gives rise to a decrease in the photocatalytic activity. This could be explained by the fact that excessive decoration of Au NPs on the surface of $CaTiO_3$ NCs could reduce the light absorption of $CaTiO_3$. The degradation percentage

of RhB after 120 min of photocatalytic reaction is inserted in Figure 9a. For the optimal composite sample—4.3%Au@CaTiO$_3$, the dye degradation reaches 99.6%, which is increased by 23.2% when compared with that for bare CaTiO$_3$ (76.4%). We also carried out the kinetic analysis of the dye degradation over the samples, as illustrated in Figure 9b. One can see that the plots of Ln(C$_t$/C$_0$) vs. *t* present a good linear relationship and can be perfectly described using the pseudo-first-order kinetic equation: Ln(C$_t$/C$_0$) = −$k_{app}t$ [69,70]. Based on the linear-regression fitting, the apparent first-order reaction rate constant k_{app} is obtained, as inserted in Figure 9b. It is concluded from the reaction rate constants (k_{app}(CaTiO$_3$) = 0.01195 min^{-1}; k_{app}(4.3%Au@CaTiO$_3$) = 0.04701 min^{-1}) that the photocatalytic activity of 4.3%Au@CaTiO$_3$ is ~3.9 times as large as that of bare CaTiO$_3$. Further comparison of the UV and visible-light photocatalytic performance between CaTiO$_3$ and 4.3%Au@CaTiO$_3$ was carried out. As shown in Figure 9c, CaTiO$_3$ exhibits an important UV photocatalytic activity toward the degradation of RhB. Moreover, a significantly enhanced UV photocatalytic activity is observed for the 4.3%Au@CaTiO$_3$ composite photocatalyst, which is ca. 3.0 times larger than that of bare CaTiO$_3$. The visible-light photocatalytic degradation of RhB over CaTiO$_3$ and 4.3%Au@CaTiO$_3$ is shown in Figure 9d. It is observed that bare CaTiO$_3$ photocatalyzes only 15.1% degradation of the dye after 120 min of photocatalysis, which could be ascribed to the dye-photosensitized degradation. This is indicative of a poor photocatalytic activity of CaTiO$_3$. Whereas 46.1% of RhB is observed to be degraded over 4.3%Au@CaTiO$_3$, implying a greatly enhanced visible-light photocatalytic activity of the composite.
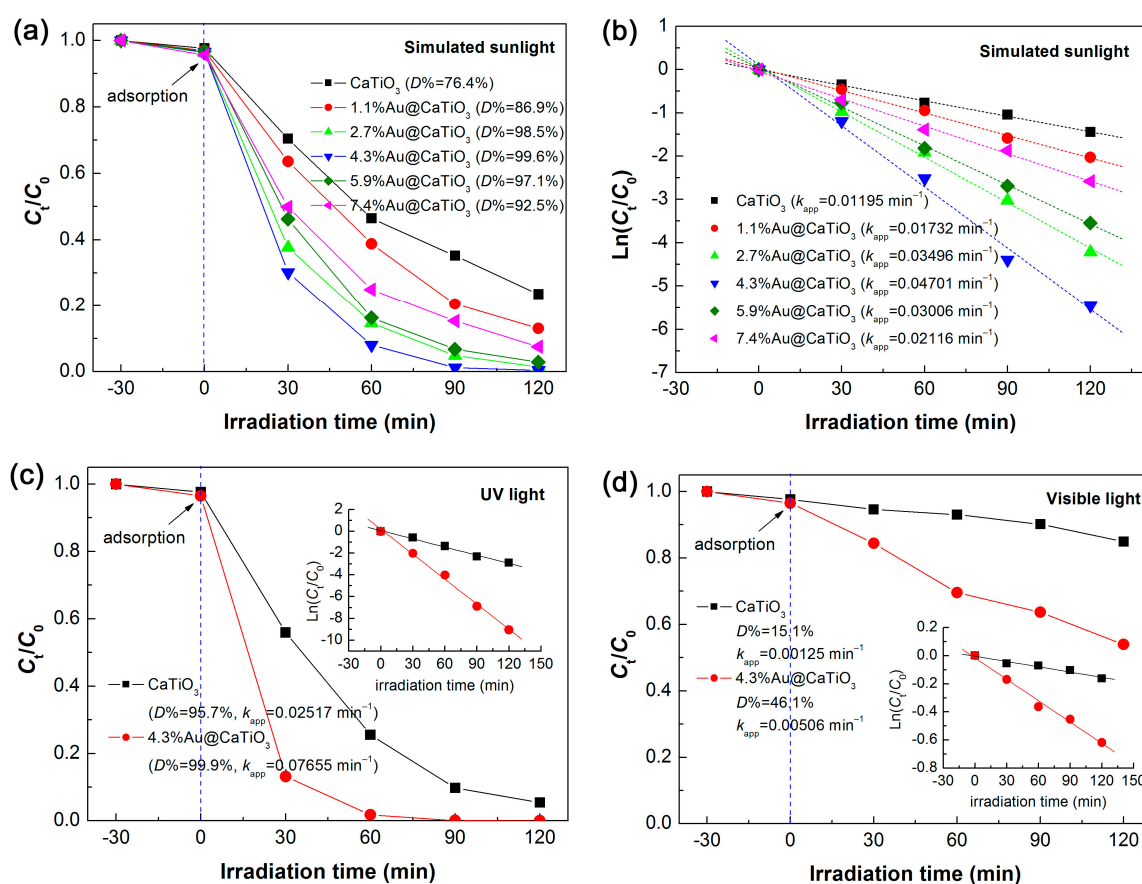

Figure 9. (**a**) Time-dependent photocatalytic degradation of RhB over bare CaTiO$_3$ and Au@CaTiO$_3$ composites under simulated sunlight irradiation. (**b**) Kinetic plots of the dye degradation over the samples under simulated sunlight irradiation. (**c**) UV and (**d**) visible-light photocatalytic degradation of RhB over bare CaTiO$_3$ and 4.3%Au@CaTiO$_3$.

Based on the above experimental results, we propose a possible mechanism to elucidate the enhanced photocatalytic performance of the Au NPs modified $CaTiO_3$ NCs, as schematically depicted Figure 10. Under UV irradiation, $CaTiO_3$ is excited to produce electrons in the CB and holes in the valence band (VB) of the semiconductor. Au NPs cannot be excited under UV irradiation, but they can act as excellent electron sinks to capture the photogenerated electrons in $CaTiO_3$. This is because the Fermi level of Au (+0.45 V vs. normal hydrogen electrode (NHE) [71,72]) is more positive than the CB potential of $CaTiO_3$ (−0.43 V vs. NHE [55]). The electron transfer process from the CB of $CaTiO_3$ to Au NPs promotes the spatial separation of the electron/hole pairs in $CaTiO_3$. This is supported by photoluminescence spectra (Figure S1), photocurrent response curves (Figure S2a) and electrochemical impedance spectroscopy (EIS) spectra (Figure S2b). As a result, more holes in the VB of $CaTiO_3$ are available for taking part in the photocatalytic reactions. Under visible-light irradiation, $CaTiO_3$ cannot be directly excited to produce electron/hole pairs, instead LSPR of Au NPs is induced by the visible-light absorption [39,40]. The LSPR-induced electrons in Au NPs could take part in the photocatalytic reactions, and moreover, the electromagnetic field caused by LSPR could stimulate the generation of electron/hole pairs in $CaTiO_3$. This is why the $Au@CaTiO_3$ composites also manifest enhanced visible-light photocatalytic degradation of RhB. When simulated sunlight is used as the light source, Au NPs simultaneously act as electron sinks and behave as LSPR effect in the $Au@CaTiO_3$ composites. The two mechanisms collectively result in the enhanced photocatalytic performance of the composites under simulated sunlight irradiation.

Hydroxyl (•OH), superoxide (•O_2^-) and h^+ are generally considered to be the main active species in most of photocatalytic systems [73]. The reactive species trapping experiments (Figure S3) reveal that the degradation of RhB is highly correlated with •OH and h^+. However, the photogenerated h^+ could not directly oxide the dye, but rather reacts with OH^- or H_2O to produce another stronger oxidant •OH. Thermodynamically •OH is ready to be generated through the reaction between h^+ and OH^-/H_2O due to the sufficiently positive VB potential of $CaTiO_3$ (+2.93 V vs. NHE [55]) when compared with the redox potentials of H_2O/•OH (+2.38 V vs. NHE) and OH^-/•OH (+1.99 V vs. NHE) [74]. •O_2^- plays only a slight role in the photocatalytic degradation of the dye. The sufficiently negative CB potential of $CaTiO_3$ (−0.43 V vs. NHE) suggests that the generation of •O_2^- can be derived from the reaction of adsorbed O_2 with the CB electrons of $CaTiO_3$ (E^0(O_2/•O_2^-) = −0.13 V vs. NHE) [74]. Moreover, the LSPR-induced electrons in Au NPs could also combine with O_2 to produce •O_2^-. Recycling photocatalytic experiment (Figure S4) is indicative of a good recycling stability of the $Au@CaTiO_3$ composite photocatalyst.

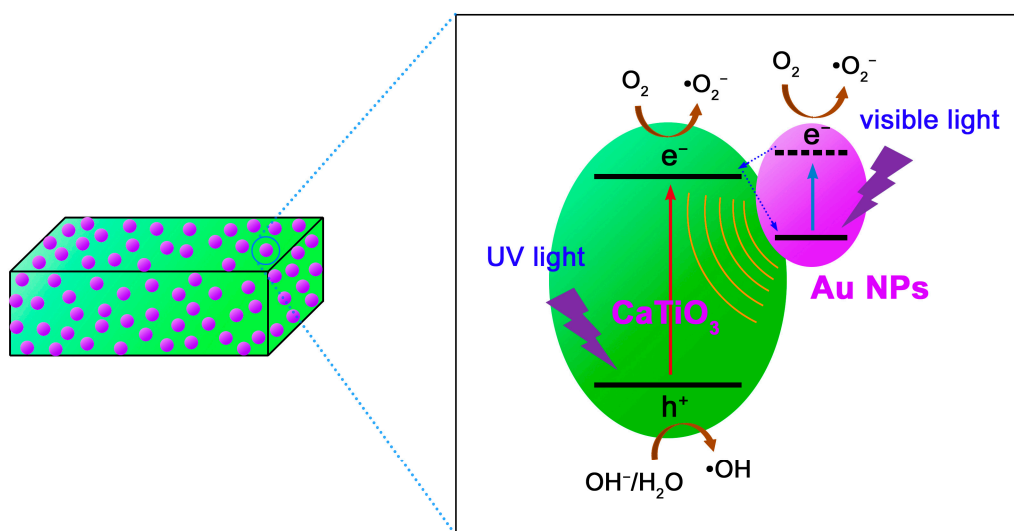**Figure 10.** Schematic illustration of the photocatalytic mechanism of the $Au@CaTiO_3$ composites.

4. Conclusions

Based on a hydrothermal route, $CaTiO_3$ NCs were synthesized using P25 as the titanium source, and their growth process was investigated by varying the reaction time. Au NPs were uniformly decorated on the $CaTiO_3$ NCs surface by a photocatalytic reduction of $HAuCl_4$ solution. Compared to bare $CaTiO_3$ NCs, the as-derived $Au@CaTiO_3$ composites manifest an increased visible-light absorption, increased photocurrent density, decreased charge-transfer resistance, decreased PL intensity, as well as enhanced photocatalytic performance for the degradation of RhB under irradiation of different light sources (simulated sunlight, UV light and visible light). The optimal composite sample, observed to be $4.3\%Au@CaTiO_3$, has a photocatalytic activity 3.9 times as large as that of bare $CaTiO_3$ NCs, and photocatalyzes 99.6% degradation of RhB under simulated sunlight irradiation for 120 min. The enhanced photocatalytic mechanism of the $Au@CaTiO_3$ composites can be explained by (1) the efficient separation of photoexcited e^-/h^+ pairs in $CaTiO_3$ due to the electron transfer from $CaTiO_3$ NCs to Au NPs, and (2) increased visible-light absorption due to the LSPR effect of Au NPs. The LSPR-caused electromagnetic field could stimulate the generation and separation of e^-/h^+ pairs in $CaTiO_3$, and moreover, the LSPR-induced electrons in Au NPs could be available for the photodegradation reactions. Reactive species trapping experiments reveal that the dye degradation is highly correlated with •OH radicals and photoexcited holes, whereas $•O_2^-$ radicals play only a slight role in the photocatalysis. The present $Au@CaTiO_3$ nanocomposite photocatalysts could offer promising applications in the design of micro/nano photocatalytic devices for the wastewater treatment.

Supplementary Materials: The following are available online at http://www.mdpi.com/2072-666X/10/4/254/s1, Figure S1. PL spectra of $CaTiO_3$ and $4.3\%Au@CaTiO_3$ measured at an excitation wavelength of 375 nm; Figure S2. (a) Transient photocurrent response curves and (b) EIS spectra of $CaTiO_3$ and $4.3\%Au@CaTiO_3$; Figure S3. Effect of ethanol, BQ and AO on the degradation of RhB over $4.3\%Au@CaTiO_3$ under simulated sunlight irradiation; Figure S4. Reusability of $4.3\%Au@CaTiO_3$ for the RhB degradation under simulated sunlight irradiation.

Author Contributions: H.Y. conceived the idea of experiment; Y.Y. performed the experiments; H.Y., Y.Y., Z.Y., R.L. and X.W. discussed the results; H.Y. wrote the manuscript; all authors read and approved the final manuscript.

Conflicts of Interest: The authors declare no conflict of interest.

References

1. Khataeea, A.R.; Kasiri, M.B. Photocatalytic degradation of organic dyes in the presence of nanostructured titanium dioxide: Influence of the chemical structure of dyes. *J. Mol. Catal. A Chem.* **2010**, *328*, 8–26. [CrossRef]

2. Brown, M.A.; De Vito, S.C. Predicting azo dye toxicity. *Crit. Rev. Environ. Sci. Technol.* **1993**, *23*, 249–324. [CrossRef]

3. Di, L.J.; Yang, H.; Xian, T.; Chen, X.J. Facile synthesis and enhanced visible-light photocatalytic activity of novel p-Ag_3PO_4/n-$BiFeO_3$ heterojunction composites for dye degradation. *Nanoscale Res. Lett.* **2018**, *13*, 257. [CrossRef]

4. Pathakoti, K.; Manubolu, M.; Hwang, H.M. Chapter 48-nanotechnology applications for environmental industry. In *Handbook of Nanomaterials for Industrial Applications*; Elsevier: Amsterdam, The Netherlands, 2018; pp. 894–907.

5. Xia, Y.M.; He, Z.M.; Yang, W.; Tang, B.; Lu, Y.L.; Hu, K.J.; Su, J.B.; Li, X.P. Effective charge separation in $BiOI/Cu_2O$ composites with enhanced photocatalytic activity. *Mater. Res. Express* **2018**, *5*, 025504. [CrossRef]

6. Rauf, M.A.; Salman Ashraf, S. Fundamental principles and application of heterogeneous photocatalytic degradation of dyes in solution. *Chem. Eng. J.* **2009**, *151*, 10–18. [CrossRef]

7. Zeng, Y.; Chen, X.F.; Yi, Z.; Yi, Y.G.; Xu, X.B. Fabrication of p-n heterostructure ZnO/Si moth-eye structures: Antireflection, enhanced charge separation and photocatalytic properties. *Appl. Surf. Sci.* **2018**, *441*, 40–48. [CrossRef]

8. Guin, J.P.; Naik, D.B.; Bhardwaj, Y.K.; Varshney, L. An insight into the effective advanced oxidation process for treatment of simulated textile dye waste water. *RSC Adv.* **2014**, *4*, 39941–39947. [CrossRef]

9. Zhao, X.X.; Yang, H.; Li, R.S.; Cui, Z.M.; Liu, X.Q. Synthesis of heterojunction photocatalysts composed of Ag_2S quantum dots combined with $Bi_4Ti_3O_{12}$ nanosheets for the degradation of dyes. *Environ. Sci. Pollut. Res. Int.* **2019**, *26*, 5524–5538. [CrossRef]

10. Xia, Y.; He, Z.; Su, J.; Liu, Y.; Tang, B. Fabrication and photocatalytic property of novel $SrTiO_3/Bi_5O_7I$ nanocomposites. *Nanoscale Res. Lett.* **2018**, *13*, 148. [CrossRef]

11. Wang, H.; Du, L.; Yang, L.L.; Zhang, W.J.; He, H.B. Sol-gel synthesis of $La_2Ti_2O_7$ modified with PEG4000 for the enhanced photocatalytic activity. *J. Adv. Oxid. Technol.* **2016**, *19*, 366–371. [CrossRef]

12. Akpan, U.G.; Hameed, B.H. Parameters affecting the photocatalytic degradation of dyes using TiO_2-based photocatalysts: A review. *J. Hazard. Mater.* **2009**, *170*, 520–529. [CrossRef]

13. Yan, Y.X.; Yang, H.; Zhao, X.X.; Li, R.S.; Wang, X.X. Enhanced photocatalytic activity of surface disorder-engineered $CaTiO_3$. *Mater. Res. Bull.* **2018**, *105*, 286–290. [CrossRef]

14. Alam, U.; Khan, A.; Raza, W.; Khan, A.; Bahnemann, D.; Muneer, M. Highly efficient Y and V co-doped ZnO photocatalyst with enhanced dye sensitized visible light photocatalytic activity. *Catal. Today* **2017**, *284*, 169–178. [CrossRef]

15. Zhang, Y.F.; Fu, F.; Li, Y.Z.; Zhang, D.S.; Chen, Y.Y. One-step synthesis of $Ag@TiO_2$ nanoparticles for enhanced photocatalytic performance. *Nanomaterials* **2018**, *8*, 1032. [CrossRef] [PubMed]

16. Zheng, C.X.; Yang, H.; Cui, Z.M.; Zhang, H.M.; Wang, X.X. A novel $Bi_4Ti_3O_{12}/Ag_3PO_4$ heterojunction photocatalyst with enhanced photocatalytic performance. *Nanoscale Res. Lett.* **2017**, *12*, 608. [CrossRef] [PubMed]

17. Xia, Y.M.; He, Z.M.; Hu, K.J.; Tang, B.; Su, J.B.; Liu, Y.; Li, X.P. Fabrication of n-$SrTiO_3$/p-Cu_2O heterojunction composites with enhanced photocatalytic performance. *J. Alloys Compd.* **2018**, *753*, 356–363. [CrossRef]

18. Wang, S.F.; Gao, H.J.; Wei, Y.; Li, Y.W.; Yang, X.H.; Fang, L.M.; Lei, L. Insight into the optical, color, photoluminescence properties, and photocatalytic activity of the N-O and C-O functional groups decorating spinel type magnesium aluminate. *CrystEngComm* **2019**, *21*, 263–277. [CrossRef]

19. Tayyebi, A.; Soltani, T.; Hong, H.; Lee, B.K. Improved photocatalytic and photoelectrochemical performance of monoclinic bismuth vanadate by surface defect states ($Bi_{1-x}VO_4$). *J. Colloid Interface Sci.* **2018**, *514*, 565–575. [CrossRef]

20. Wang, S.Y.; Yang, H.; Wang, X.X.; Feng, W.J. Surface disorder engineering of flake-like Bi_2WO_6 crystals for enhanced photocatalytic activity. *J. Electron. Mater.* **2019**, *48*, 2067–2076. [CrossRef]

21. Wang, X.X.; Wu, X.X.; Zhu, J.K.; Pang, Z.Y.; Yang, H.; Qi, Y.P. Theoretical investigation of a highly sensitive refractive-index sensor based on TM0 waveguide mode resonance excited in an asymmetric metal-cladding dielectric waveguide structure. *Sensors* **2019**, *19*, 1187. [CrossRef]

22. Fernando, K.A.S.; Sahu, S.P.; Liu, Y.; Lewis, W.K.; Guliants, E.; Jafariyan, A.; Wang, P.; Bunker, C.E.; Sun, Y.P. Carbon quantum dots and applications in photocatalytic energy conversion. *ACS Appl. Mater. Interfaces* **2015**, *7*, 8363–8376. [CrossRef]

23. Devil, P.; Thakur, A.; Bhardwaj, S.K.; Saini, S.; Rajput, P.; Kumar, P. Metal ion sensing and light activated antimicrobial activity of aloevera derived carbon dots. *J. Mater. Sci.-Mater. Electron.* **2018**, *29*, 17254–17261. [CrossRef]

24. Yi, Z.; Liu, L.; Wang, L.; Cen, C.; Chen, X.; Zhou, Z.; Ye, X.; Yi, Y.; Tang, Y.; Yi, Y.; et al. Tunable dual-band perfect absorber consisting of periodic cross-cross monolayer graphene arrays. *Results Phys.* **2019**, *13*, 102217. [CrossRef]

25. Wang, X.X.; Tong, H.; Pang, Z.Y.; Zhu, J.K.; Wu, X.X.; Yang, H.; Qi, Y.P. Theoretical realization of three-dimensional nanolattice structure fabrication based on high-order waveguide-mode interference and sample rotation. *Opt. Quantum Electron.* **2019**, *51*, 38. [CrossRef]

26. Wang, X.X.; Zhu, J.K.; Tong, H.; Yang, X.D.; Wu, X.X.; Pang, Z.Y.; Yang, H.; Qi, Y.P. A theoretical study of a plasmonic sensor comprising a gold nano-disk array on gold film with an SiO_2 spacer. *Chin. Phys. B* **2019**, *28*, 044201. [CrossRef]

27. Liu, L.; Chen, J.J.; Zhou, Z.G.; Yi, Z.; Ye, X. Tunable absorption enhancement in electric split-ring resonators-shaped graphene array. *Mater. Res. Express* **2018**, *5*, 045802. [CrossRef]

28. Cen, C.L.; Chen, J.J.; Liang, C.P.; Huang, J.; Chen, X.F.; Tang, Y.J.; Yi, Z.; Xu, X.B.; Yi, Y.G.; Xiao, S.Y. Plasmonic absorption characteristics based on dumbbell-shaped graphene metamaterial arrays. *Phys. E* **2018**, *103*, 93–98. [CrossRef]

29.   Yi, Z.; Lin, H.; Niu, G.; Chen, X.F.; Zhou, Z.G.; Ye, X.; Duan, T.; Yi, Y.; Tang, Y.J.; Yi, Y.G. triple-band plasmonic perfect metamaterial absorber with good angle-polarization-tolerance. *Results Phys.* **2019**, *13*, 102149. [CrossRef]

30.   Yi, Z.; Chen, J.J.; Cen, C.L.; Chen, X.F.; Zhou, Z.G.; Tang, Y.J.; Ye, X.; Xiao, S.Y.; Luo, W.; Wu, P.H. Tunable graphene-based plasmonic perfect metamaterial absorber in the THz region. *Micromachines* **2019**, *10*, 194. [CrossRef]

31.   Wang, X.X.; Bai, X.L.; Pang, Z.Y.; Zhu, J.K.; Wu, Y.; Yang, H.; Qi, Y.P.; Wen, X.L. Surface-enhanced Raman scattering by composite structure of gold nanocube-PMMA-gold film. *Opt. Mater. Express* **2019**, *9*, 1872–1881. [CrossRef]

32.   Wang, X.X.; Pang, Z.Y.; Tong, H.; Wu, X.X.; Bai, X.L.; Yang, H.; Wen, X.L.; Qi, Y.P. Theoretical investigation of subwavelength structure fabrication based on multi-exposure surface plasmon interference lithography. *Results Phys.* **2019**, *12*, 732–737. [CrossRef]

33.   Huang, J.; Niu, G.; Yi, Z.; Chen, X.F.; Zhou, Z.G.; Ye, X.; Tang, Y.J.; Duan, T.; Yi, Y.; Yi, Y.G. High sensitivity refractive index sensing with good angle and polarization tolerance using elliptical nanodisk graphene metamaterials. *Phys. Scr.* **2019**, in press. [CrossRef]

34.   Zhao, X.X.; Yang, H.; Cui, Z.M.; Wang, X.X.; Yi, Z. Growth process and CQDs-modified $Bi_4Ti_3O_{12}$ square plates with enhanced photocatalytic performance. *Micromachines* **2019**, *10*, 66. [CrossRef]

35.   Mahdiani, M.; Soofivand, F.; Ansari, F.; Salavati-Niasari, M. Grafting of $CuFe_{12}O_{19}$ nanoparticles on CNT and graphene: Eco-friendly synthesis, characterization and photocatalytic activity. *J. Clean. Prod.* **2018**, *176*, 1185–1197. [CrossRef]

36.   Cruz-Ortiz, B.R.; Hamilton, J.W.J.; Pablos, C.; Diaz-Jimenez, L.; Cortes-Hernandez, D.A.; Sharma, P.K.; Castro-Alferez, M.; Fernandez-Ibanez, P.; Dunlop, P.S.M.; Byrne, J.A. Mechanism of photocatalytic disinfection using titania-graphene composites under UV and visible irradiation. *Chem. Eng. J.* **2017**, *316*, 179–186. [CrossRef]

37.   Di, L.J.; Yang, H.; Xian, T.; Chen, X.J. Construction of Z-scheme $g-C_3N_4/CNT/Bi_2Fe_4O_9$ composites with improved simulated-sunlight photocatalytic activity for the dye degradation. *Micromachines* **2018**, *9*, 613. [CrossRef]

38.   Ji, K.M.; Deng, J.G.; Zang, H.J.; Han, J.H.; Arandiyan, H.; Dai, H.X. Fabrication and high photocatalytic performance of noble metal nanoparticles supported on 3DOM $InVO_4$-$BiVO_4$ for the visible-light-driven degradation of rhodamine B and methylene blue. *Appl. Catal. B-Environ.* **2015**, *165*, 285–295. [CrossRef]

39.   Lee, J.E.; Bera, S.; Choi, Y.S.; Lee, W.I. Size-dependent plasmonic effects of M and $M@SiO_2$ (M = Au or Ag) deposited on TiO_2 in photocatalytic oxidation reactions. *Appl. Catal. B-Environ.* **2017**, *214*, 15–22. [CrossRef]

40.   She, P.; Xu, K.L.; Zeng, S.; He, Q.R.; Sun, H.; Liu, Z.N. Investigating the size effect of Au nanospheres on the photocatalytic activity of Au-modified ZnO nanorods. *J. Colloid Interface Sci.* **2017**, *499*, 76–82. [CrossRef]

41.   Pang, Z.Y.; Tong, H.; Wu, X.X.; Zhu, J.K.; Wang, X.X.; Yang, H.; Qi, Y.P. Theoretical study of multiexposure zeroth-order waveguide mode interference lithography. *Opt. Quantum Electron.* **2018**, *50*, 335. [CrossRef]

42.   Wang, X.X.; Bai, X.L.; Pang, Z.Y.; Yang, H.; Qi, Y.P. Investigation of surface plasmons in Kretschmann structure loaded with a silver nano-cube. *Results Phys.* **2019**, *12*, 1866–1870. [CrossRef]

43.   Biegalski, M.D.; Qiao, L.; Gu, Y.; Mehta, A.; He, Q.; Takamura, Y.; Borisevich, A.; Chen, L.Q. Impact of symmetry on the ferroelectric properties of $CaTiO_3$ thin films. *Appl. Phys. Lett.* **2015**, *106*, 162904. [CrossRef]

44.   Zhu, X.N.; Gao, T.T.; Xu, X.; Liang, W.Z.; Lin, Y.; Chen, C.; Chen, X.M. Piezoelectric and dielectric properties of multilayered $BaTiO_3/(Ba,Ca)TiO_3/CaTiO_3$ thin films. *ACS Appl. Mater. Interfaces* **2016**, *8*, 22309–22315. [CrossRef]

45.   Tariq, S.; Ahmed, A.; Saad, S.; Tariq, S. Structural, electronic and elastic properties of the cubic $CaTiO_3$ under pressure: A DFT study. *AIP Adv.* **2015**, *5*, 77111. [CrossRef]

46.   Shi, X.; Yang, H.; Liang, Z.; Tian, A.; Xue, X. Synthesis of vertically aligned $CaTiO_3$ nanotubes with simple hydrothermal method and its photoelectrochemical property. *Nanotechnology.* **2018**, *29*, 385605. [CrossRef]

47.   Yan, X.; Huang, X.J.; Fang, Y.; Min, Y.H.; Wu, Z.J.; Li, W.S.; Yuan, J.M.; Tan, L.G. Synthesis of rodlike $CaTiO_3$ with enhanced charge separation efficiency and high photocatalytic activity. *Int. J. Electrochem. Sci.* **2014**, *9*, 5155–5163.

48.   Lim, S.N.; Song, S.A.; Jeong, Y.C.; Kang, H.W.; Park, S.B.; Kim, K.Y. H_2 production under visible light irradiation from aqueous methanol solution on $CaTiO_3$:Cu prepared by spray pyrolysis. *J. Electron. Mater.* **2017**, *46*, 6096–6103. [CrossRef]

49. Dong, W.X.; Song, B.; Zhao, G.L.; Meng, W.J.; Han, G.R. Effects of the volume ratio of water and ethanol on morphosynthesis and photocatalytic activity of $CaTiO_3$ by a solvothermal process. *Appl. Phys. A* **2017**, *123*, 348. [CrossRef]

50. Alammara, T.; Hamma, I.; Warkb, M.; Mudring, A.V. Low-temperature route to metal titanate perovskite nanoparticles for photocatalytic applications. *Appl. Catal. B-Environ.* **2015**, *178*, 20–28. [CrossRef]

51. Kimijima, T.; Kanie, K.; Nakaya, M.; Muramatsu, A. Hydrothermal synthesis of size- and shape-controlled $CaTiO_3$ fine particles and their photocatalytic activity. *CrystEngComm* **2014**, *16*, 5591–5597. [CrossRef]

52. Ye, M.; Wang, M.; Zheng, D.; Zhang, N.; Lin, C.; Lin, Z. Garden-like perovskite superstructures with enhanced photocatalytic activity. *Nanoscale* **2014**, *6*, 3576–3584. [CrossRef]

53. Zhao, X.X.; Yang, H.; Li, S.H.; Cui, Z.M.; Zhang, C.R. Synthesis and theoretical study of large-sized $Bi_4Ti_3O_{12}$ square nanosheets with high photocatalytic activity. *Mater. Res. Bull.* **2018**, *107*, 180–188. [CrossRef]

54. Pan, J.; Liu, G.; Lu, G.Q.; Cheng, H.M. On the true photoreactivity order of {001}, {010}, and {101} facets of anatase TiO_2 crystals. *Angew. Chem. Int. Ed.* **2011**, *50*, 2133–2137. [CrossRef]

55. Yan, Y.X.; Yang, H.; Zhao, X.X.; Zhang, H.M.; Jiang, J.L. A hydrothermal route to the synthesis of $CaTiO_3$ nanocuboids using P25 as the titanium source. *J. Electron. Mater.* **2018**, *47*, 3045–3050. [CrossRef]

56. Bai, L.Y.; Xu, Q.; Cai, Z.S. Synthesis of $Ag@AgBr/CaTiO_3$ composite photocatalyst with enhanced visible light photocatalytic activity. *J. Mater. Sci.-Mater. Electron.* **2018**, *29*, 17580–17590. [CrossRef]

57. Alzahrani, A.; Barbash, D.; Samokhvalov, A. "One-pot" synthesis and photocatalytic hydrogen generation with nanocrystalline $Ag(0)/CaTiO_3$ and in situ mechanistic studies. *J. Phys. Chem. C* **2016**, *120*, 19970–19979. [CrossRef]

58. Jiang, Z.Y.; Pan, J.Q.; Wang, B.B.; Li, C.R. Two dimensional Z-scheme $AgCl/Ag/CaTiO_3$ nano-heterojunctions for photocatalytic hydrogen production enhancement. *Appl. Surf. Sci.* **2018**, *436*, 519–526. [CrossRef]

59. Yang, J.J.; Jin, Z.S.; Wang, X.D.; Li, W.; Zhang, J.W.; Zhang, S.L.; Guo, X.Y.; Zhang, Z.J. Study on composition, structure and formation process of nanotube $Na_2Ti_2O_4(OH)_2$. *Dalton Trans.* **2003**, 3898–3901. [CrossRef]

60. Durrania, S.K.; Khan, Y.; Ahmed, N.; Ahmad, M.; Hussain, M.A. Hydrothermal growth of calcium titanate nanowires from titania. *J. Iran. Chem. Soc.* **2011**, *8*, 562–569. [CrossRef]

61. Zheng, C.X.; Yang, H. Assembly of Ag_3PO_4 nanoparticles on rose flower-like Bi_2WO_6 hierarchical architectures for achieving high photocatalytic performance. *J. Mater. Sci.-Mater. Electron.* **2018**, *29*, 9291–9300. [CrossRef]

62. Pooladi, M.; Shokrollahi, H.; Lavasani, S.A.N.H.; Yang, H. Investigation of the structural, magnetic and dielectric properties of Mn-doped $Bi_2Fe_4O_9$ produced by reverse chemical co-precipitation. *Mater. Chem. Phys.* **2019**, *229*, 39–48. [CrossRef]

63. Camci, M.T.; Ulgut, B.; Kocabas, C.; Suzer, S. In-situ XPS monitoring and characterization of electrochemically prepared Au nanoparticles in an ionic liquid. *ACS Omega* **2017**, *2*, 478–486. [CrossRef] [PubMed]

64. Gao, H.J.; Wang, F.; Wang, S.F.; Wang, X.X.; Yi, Z.; Yang, H. Photocatalytic activity tuning in a novel $Ag_2S/CQDs/CuBi_2O_4$ composite: Synthesis and photocatalytic mechanism. *Mater. Res. Bull.* **2019**, *115*, 140–149. [CrossRef]

65. Wang, Y.; Niu, C.G.; Wang, L.; Wang, Y.; Zhang, X.G.; Zeng, G.M. Synthesis of fern-like $Ag/AgCl/CaTiO_3$ plasmonic photocatalysts and their enhanced visible-light photocatalytic properties. *RSC Adv.* **2016**, *6*, 47873–47882. [CrossRef]

66. Roy, A.S.; Hegde, S.G.; Parveen, A. Synthesis, characterization, AC conductivity, and diode properties of polyaniline–$CaTiO_3$ composites. *Polym. Adv. Technol.* **2014**, *25*, 130–135. [CrossRef]

67. Wang, S.F.; Gao, H.J.; Fang, L.M.; Wei, Y.; Li, Y.W.; Lei, L. Synthesis and characterization of $BaAl_2O_4$ catalyst and its photocatalytic activity towards degradation of methylene blue dye. *Z. Phys. Chem.* **2019**. [CrossRef]

68. Mert, B.D.; Mert, M.E.; Kardas, G.; Yazici, B. Experimental and theoretical studies on electrochemical synthesis of poly(3-amino-1,2,4-triazole). *Appl. Surf. Sci.* **2012**, *258*, 9668–9674. [CrossRef]

69. Ye, Y.C.; Yang, H.; Zhang, H.M.; Jiang, J.L. A promising $Ag_2CrO_4/LaFeO_3$ heterojunction photocatalyst applied to photo-Fenton degradation of RhB. *Environ. Technol.* **2018**, 1–18. [CrossRef]

70. Konstantinou, I.K.; Albanis, T.A. TiO_2-assisted photocatalytic degradation of azo dyes in aqueous solution: Kinetic and mechanistic investigations: A review. *Appl. Catal. B-Environ.* **2004**, *49*, 1–14. [CrossRef]

71. Subramanian, V.; Wolf, E.E.; Kamat, P.V. Catalysis with TiO_2/Gold nanocomposites: Effect of metal particle size on the Fermi level equilibration. *J. Am. Chem. Soc.* **2004**, *126*, 4943–4950. [CrossRef]

72. Zheng, C.X.; Yang, H.; Cui, Z.M. Enhanced photocatalytic performance of Au nanoparticles-modified rose flower-like Bi_2WO_6 hierarchical architectures. *J. Ceram. Soc. Jpn.* **2017**, *125*, 887–893. [CrossRef]

73. Zhao, X.X.; Yang, H.; Zhang, H.M.; Cui, Z.M.; Feng, W.J. Surface-disorder-engineering-induced enhancement in the photocatalytic activity of $Bi_4Ti_3O_{12}$ nanosheets. *Desalin. Water Treat.* **2019**, *145*, 326–336. [CrossRef]

74. Di, L.J.; Yang, H.; Xian, T.; Liu, X.Q.; Chen, X.J. Photocatalytic and photo-Fenton catalytic degradation activities of Z-scheme $Ag_2S/BiFeO_3$ heterojunction composites under visible-light irradiation. *Nanomaterials* **2019**, *9*, 399. [CrossRef] [PubMed]